




Received 13 July 2022; revised 9 September 2022 and 16 October 2022; accepted 31 October 2022. Date of publication 14 November 2022; date of current version 5 July 2023.

Digital Object Identifier 10.1109/OJSSCS.2022.3221924

A Review of Electrochemical Electrodes and Readout Interface Designs for Biosensors

YUAN MA¹, YUPING DENG², CHAO XIE¹, BINGJING ZHANG¹, BOYU SHEN²,
MILIN ZHANG^{1,3}  (Senior Member, IEEE), LAN YIN², XILIN LIU⁴  (Senior Member, IEEE),
AND JAN VAN DER SPIEGEL⁵  (Life Fellow, IEEE)

¹Department of Electronic Engineering, Tsinghua University, Beijing 100084, China

²School of Materials Science and Engineering, Tsinghua University, Beijing 100084, China

³Beijing National Research Center for Information Science and Technology, Institute for Precision Medicine, Tsinghua University, Beijing 100084, China

⁴Department of Electrical and Computer Engineering, University of Toronto, Toronto, ON M5S 3G4, Canada

⁵Department of Electrical and Systems Engineering, University of Pennsylvania, Philadelphia, PA 19104, USA

CORRESPONDING AUTHOR: M. ZHANG (e-mail: zhangmilin@tsinghua.edu.cn)

This work was supported in part by the Natural Science Foundation of China under Grant 92164202, and in part by the Beijing Innovation Center for Future Chip.

(Yuan Ma and Yuping Deng contributed equally to this work.)

ABSTRACT Electrochemical detection is widely used in biosensing fields, such as medical diagnosis and health monitoring due to its real-time response and high accuracy. Both passive and active electrodes and the corresponding readout circuits have been continuously improved over the past decades. This article summarizes the redox reaction method, state-of-the-art electrode materials, and readout circuits based on the passive three-electrode. The redox-current-based readout circuits are widely used and developed toward multichannel high precision and low power consumption. In terms of active electrodes, this article reviews the development of field-effect transistors (FETs)-based electrochemical detection and readout circuits. In the past decade, the development of organic electrochemical transistors (OECTs) has also enabled more precise electrochemical detection.

INDEX TERMS Ion-selective field-effect transistor (ISFET), organic electrochemical transistor (OECT), potentiostat, three-electrode system, transimpedance amplifier (TIA).

I. INTRODUCTION

ELECTROCHEMICAL detection is widely used in medical diagnosis and health monitoring due to its real-time response and high accuracy. Accurate and real-time electrochemical continuous detection is required for drug guidance, surgical intervention plans, and postoperative monitoring [1], [2]. In addition, electrochemical detection is also widely used for the daily health detection, such as sweat analysis [3], [4] and blood monitoring [5], [6], [7], [8].

An electrochemical detector consists of an electrochemical interface and a readout interface. The electrochemical interface acts as a transducer to convert chemical specification into electronic indicators, such as changes in potential, current, or impedance. The readout interface is used to bias the current and potential required by the electrochemical interface and to readout the converted electrical indicators.

The principles of a typical electrochemical interface include redox reactions and target adsorption [9]. For redox-reaction-based electrochemical interface, the oxidation and reduction reactions occur each at two electrodes, which are called the working electrode (WE) and the counter electrode (CE), respectively. With a fixed current bias, the WE's potential is proportional to the concentration of the analyte, which can be readout directly by readout circuits. The CE is usually an inert electrode that provides a reference. However, limited by current control requirements, the potential readout circuit suffers from a low sensitivity, which limits its application potentials [10]. In recent years, current readout circuits typically utilize a three-electrode system to detect the Faradaic currents generated by electron exchange during redox reactions. In addition to the WE and CE where redox reactions take place, a reference electrode (RE) is added to

provide a stable and constant potential. The designs of the three-electrode system have been continuously optimized for lower cost, faster speed, and higher accuracy [11], [12], [13], [14], [15].

On the other hand, the impedance of an adsorption-based transducer changes by absorbing or binding target molecules to the transducer. The readout circuits for applying voltage and finding current are widely used as the impedance readout interface. The adsorption-based transducer has been used in transistor designs which turns the concentration into the changes of the transistor's threshold voltage or channel conductivity. A typical representative is the ion-selective field-effect transistor (ISFET). Benefiting from the high integration levels guaranteed by the process, readout circuits of ISFET are becoming fully integrated systems [16]. ISFET-based sensing is widely used for ion imaging [17], [18] and DNA sequencing [19], [20], [21]. In the past decade, breakthroughs in organic electrochemical transistors (OECTs) have also enabled electrochemical detection with higher precision [22], [23], [24]. However, certain challenges of these electrochemical sensors still remain unanswered. From a technological point of view, the main challenges are related to the enhancement of their sensing performance (robustness, selectivity, sensitivity, reliability, etc.) and the reduction of their dimensions and power consumption. Although nano-materials provide decent electrochemical and mechanical properties [25], they still suffer from electrical instability since it is difficult to control the number, size, and shape of their nanostructures [26]. Efforts should also be made for optimizing the flexibility and stretchability of wearable electronics to provide intimate integration to soft tissues and overcome potential inflammatory response [27]. In addition, a more reliable electrode system with its corresponding readout interface and packaging strategy will improve the long-term stability of these devices in liquid environments. In the future, advanced material strategies and circuit designs will hold great promise for improving the performance of these electrochemical systems.

The remainder of this article is organized as follows. Section II introduces the redox-reaction-based electrochemical interface and the corresponding three-electrode-based readout interface circuits. Section III introduces the development of ISFETs and OECTs and the follow-up of the readout interface circuits. Section IV concludes the entire work.

II. REDOX-BASED ELECTROCHEMICAL INTERFACE

A. REDOX MEASUREMENT PRINCIPLES

As shown in Fig. 1(a), when controlling the redox current, I_{redox} , one can readout the potential V_{cell} , which allows the calculation of species concentrations. The voltage between WE and RE is denoted as V_{cell} , which is related to the analyte concentrations and is described by the Nernst equation [29]

$$V_{\text{cell}} = V_{\text{cell}}^0 + \frac{RT}{nF} \ln\left(\frac{[\text{Red}]}{[\text{Oxi}]}\right) \quad (1)$$

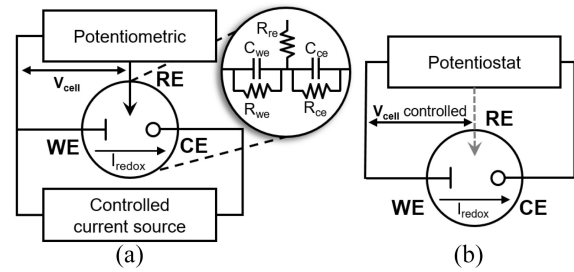


FIGURE 1. Experimental arrangement for (a) potential-readout and (b) current-readout experiments (adapted from [28]).

where V_{cell}^0 is the standard potential of a half-reaction, R is the universal gas constant, T is the absolute temperature, and n is the number of electrons involved in the half-reaction and F is Faraday's constant. $[\text{Red}]$ equals the activity of the reduced species. $[\text{Oxi}]$ equals the activity of the oxidized species. However, the interference of the charging current of the electrode-solution interface double-layer capacitor C_{we} is difficult to be filtered out, which results in low sensitivity [28].

Fig. 1(b) shows the experimental arrangement for current-readout experiments. When the bias circuit at RE has a large impedance, the current flowing through R_{re} is almost 0. The RE provides a stable and constant potential compared to the WE and avoids the deterioration of the sensing performance. The current generated by redox reactions is directly proportional to the concentration of the analyte. The correlated current flow can be described by the Cottrell equation as shown in the following [30]:

$$I_{\text{redox}} = nFAc\sqrt{\frac{D}{\pi t}} \quad (2)$$

where I_{redox} is the current at time t . n is the number of electrons involved in the reaction. F is Faraday's constant, A is the geometric area of the WE, c is the concentration of the oxidized species, and D is the diffusion coefficient of the oxidized species.

In general, amperometric and voltammetric techniques are the most common methods used to trace the variation of the redox current. Amperometric sensors depend on the continuously current measurement stimulated by a stable potential controlled of V_{cell} . As one of the most commonly used type of electrochemical sensors, amperometric sensors exhibit rapid robustness, excellent sensitivity, and low detection limit, which is the smallest amount of the analyte that can be reliably detected by the device [31]. However, interfering species that have lower oxidation potentials than the applied voltage could be oxidized during the measurement, causing the amperometric sensors to suffer from poor selectivity [9].

In voltammetric sensors, electrochemical characteristics of the analyte are collected by measuring the current over a controlled variation of the applied voltages [32]. For example, the potential at which the target analyte begins to be oxidized or reduced can be recorded via voltage sweeping when the resultant current shows a peak or trough due to the mass

TABLE 1. Summary of recent electrochemical sensors of electroactive biomarkers.

Ref.	Target Analytes	Half-life	Sensor Materials	Measured Range
[36]	Dopamine	ms-s	MnO ₂ NWs/ErGO/GCE	0.01 -80 μ M
[37]	Dopamine	ms-s	GQDs-MWCNTs	0.005-100.0 μ M
[38]	Dopamine	ms-s	PtNi@MoS ₂ /GCE	0.5-600 μ M
[39]	Dopamine	ms-s	MIPs/pThi/NPG	0.3-100 μ M
[2]	Nitric Oxide(NO)	0.1-10 s	PLLA-PTMC/Au/poly(eugenol)	0.01-100 μ M
[40]	Epinephrine	1-3 min	ZnO/MWCNTs/GCE	0.4-2.4 μ M
[41]	Norepinephrine	1-3 min	GCE/GQD/AuNPs	0.5-7.5 μ M
[41]	Lactate	2-5 min (with physical activities) 20-60 min (normal level)	MIPs/AgNWs	0.001-100 mM
[42]	Glucose	~20 min	Ni-BDC/MOF	0.01-0.8 mM
[43]	Glucose	~20 min	Au-Ni/pTBA	1.0 μ M-30.0 mM
[44]	Glucose	~20 min	NPG/PUNFs/PDMS	0.02-0.6 mM
[45]	Glucose	~20 min	Cu-MOF/MWNTs/GCE	0.5 μ M-11.84 mM
[46]	Glutathione	6-8 min	Ag/Cu-TCPP/GCE	0.001-0.1 mM
[47]	Nitrite	20-45 min	AgNWs/IDE-rGO	5-50 ppm
[48]	Nitrite	20-45 min	PEDOT:PSS/WO ₃	10-80 ppm
[49]	Nitrate	5-8 h	CF@CuNiAl/LDHs	5 nM-40 μ M 75 μ M-2.4 mM

transport effect. Different time–voltage relationships result in different voltage shapes including linear sweep voltammetry (LSV), cyclic voltammetry (CV), differential pulse voltammetry (DPV), and square-wave voltammetry (SWV). In LSV, voltage is scanned from a lower limit to an upper limit in only one direction (either positive or negative) with a preset sweeping rate. CV changes the sweep direction at a fixed rate between two values to generate cycles, in which case the target analyte may undergo multiple redox cycles. Therefore, a reversible electrochemical process recorded by CV has a well-defined feature. CV is a powerful electrochemical technique widely used for investigating the redox processes and relevant characteristics (e.g., redox potentials and electrochemical rate constant) involved in the electrochemical reaction of interests [33]. DPV can be used to obtain accurate and reproducible values of the redox potential with higher selectivity and sensitivity. In the DPV experiment, the amplitude of the current is measured in a forward pulse and a reverse pulse, and the current difference between the forward and reverse pulses is recorded. Therefore, the influence of capacitor current is minimized by the subtraction of current [34]. SWV derives the I–V characteristics from the application of the potential in the form of rectangular waves. SWV can achieve better capacitor current suppression for higher sensitivity while requiring less time per scan than DPV [35].

B. ELECTRODE MATERIALS

As redox reactions only occur at the surface of the WE, materials have a significant impact on the performance of the electrochemical analysis. Typically, these materials should exhibit ideal electrical conductivity, chemical inertness, mechanical properties, and low background current resulting from redox reaction under the applied potential. Noble metals (Au, Pt, Ag, Pd, etc.), and carbon-based materials (glassy carbon, carbon nanotubes, graphene, carbon nanofibers, etc.), metal–oxides (ZnO, WO₃, TiO₂, CeO₂, etc.) are the main materials used for WEs [50], [51]. Other

2-D nanomaterials, such as black phosphorus (BP), MXenes, and transition metal dichalcogenides (TMDCs) which have high electroactive surface area, have also shown significant improvement in performance of sensors [52], [53]. In addition, some efforts have been made on the modification of the WEs to achieve fast electron transfer kinetics, increased sensitivity and selectivity and stable electrode surfaces [54]. Inert conducting materials (e.g., platinum or graphite) are often utilized as CE and the normal hydrogen electrode (NHE), saturated calomel electrode (SCE), and saturated silver/silver chloride electrode (Ag/AgCl) are most commonly used for REs.

Based on these materials, electrochemical sensors have wide applications in health care, disease diagnosis, environmental monitoring, food evaluation, and drug delivery by identifying or detecting biomarkers of interest (e.g., dopamine, nitric oxide, glucose, lactate, etc.). Table 1 presents the list of recent electrochemical sensors, materials, target analytes, and the detection range. However, it still remains a challenge to accurately monitor these biomarkers in biological systems since their concentrations significantly vary in different organs or tissues [55] and most of them exhibit a short half-life time ranging from milliseconds to minutes.

III. THREE-ELECTRODE BASED READOUT INTERFACE

The readout interface used for voltage (V_{cell}) biasing and current (I_{redox}) readout in a three-electrode system is called a potentiostat. Typical three-electrode potentiostats include a resistance feedback TIA (R-TIA), a capacitance feedback TIA (C-TIA), and the current mirror (CM) circuits. R-TIAs and C-TIAs circuits convert read redox currents to voltages and ADCs are used for conversion from analog voltages to digital signals. As for the CM circuits, after mirroring the current to be measured, the current is converted into frequency or other electrical parameters. The TDCs are used to quantize time signals into digital signals.

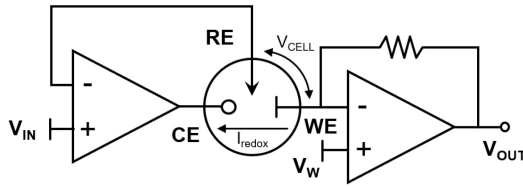


FIGURE 2. Single-ended potentiostat with the WE is connected to the virtual ground.

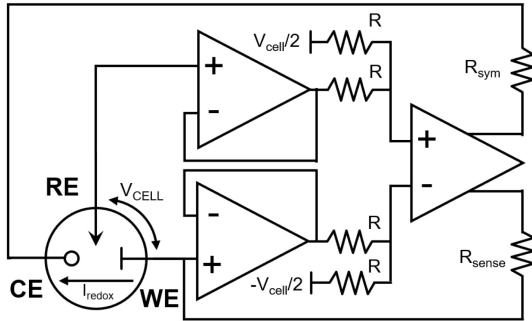


FIGURE 3. Fully differential potentiostat (adapted from [56]).

A. RESISTIVE FEEDBACK CURRENT READOUT CIRCUITS

The most popular resistive feedback potentiostat is a single-ended circuit, as shown in Fig. 2. The electrochemical reaction potential $V_{\text{cell}} = V_{\text{WE}} - V_{\text{RE}}$. The potential of WE, V_{WE} , is connected to the virtual ground, while the potential of RE, V_{RE} , follows the applied voltage V_{IN} . Thus, the value of V_{cell} changes with V_{IN} . The output voltage V_{out} is proportional to the redox current I_{redox} and the feedback resistance. The readout of small currents requires a high conversion gain for the R-TIA. For example, an input current of 1 pA requires a 1-G Ω resistor to reach 1-mV output, which is difficult to be implemented in standard complementary metal–oxide–semiconductor (CMOS).

Potentiostats need to be able to provide output voltages of different magnitudes for different chemical analytes. However, the operation of a single-ended potentiostat is limited by the swing of the control amplifier for low-supply voltage chip applications and can be affected by common-mode interference. In order to adapt to various scenarios and solve the problem of small output swing of single-ended potentiostats in low-voltage applications, Ghodsevali et al. [56] and Martin et al. [57] proposed the potentiostat with a fully differential structure, as shown in Fig. 3. R_{sense} is used as a current sampling resistor, and R_{sym} keeps the circuit structure symmetrical. This structure nearly doubles the output swing of the voltage-controlled amplifier, as shown in

$$S_{\text{FD}} = 2|V_{\text{DD}} - V_{\text{SS}}| \frac{R_{\text{we}}}{R_{\text{we}} + 2R_{\text{sym}} + R_{\text{ce}}}. \quad (3)$$

This allows the potentiostat to accommodate a larger dynamic output range of the sensor. In addition, the fully differential structure can better suppress common mode noise.

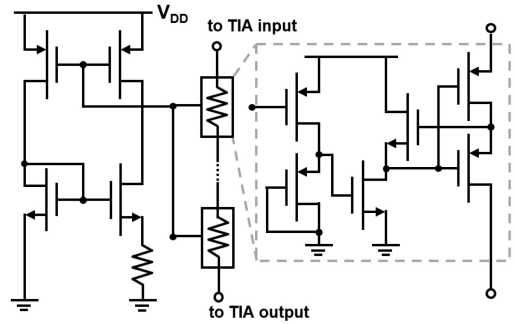


FIGURE 4. Schematic of the pseudo-resistor elements in series (adapted from [58]).

This structure is difficult to apply to the detection of small currents. R_{sense} should not be too large to reduce the voltage drop. Besides, R_{sense} and R_{sym} are directly connected in series in the WE and CE loops, and their thermal noise introduces a large input error.

In order to integrate large resistors on-chip, a pseudo-resistor can be considered. The traditional pseudo-resistor structure consists of two back-to-back MOS transistors as diodes. When they work in the weak inversion region and there is no dc current, a high equivalent resistance value can be achieved. However, the PVT (process, voltage, and temperature) robustness of traditional pseudo-resistors is poor. Besides, when the dc current is nonzero, the noise performance is worse than that of normal resistors. Therefore, Djekic et al. [58] proposed an improved pseudo-resistive feedback TIA, as shown in Fig. 4. Djekic et al. [58] described a method of connecting pseudo-resistance elements in series to reduce mismatch and improve the linearity by reducing the voltage drop over the pseudo-resistance unit. At the same time, the series connection of pseudo-resistor elements forces it to work in the linear region to reduce the spurious noise. The silicon on insulator (SOI) technology reduces parasitic effects and alleviate stability problems. The transimpedance value can be adjusted between 1 M Ω and 1 G Ω with corresponding bandwidths from 8 kHz to 2 MHz. The 1-M Ω transimpedance change is less than 10% over a temperature range from -40°C to 125°C .

B. CAPACITIVE FEEDBACK CURRENT READOUT CIRCUITS

In order to realize an integrated low-noise potentiostat, another common practice is to use C-TIA to form an integrator-differentiator structure. Compared with the R-TIA with limited resistance size, the C-TIA potentiostat is not limited by resistance thermal noise, and the input equivalent noise can be lower [8], [59]. But the leakage current at the input node will cause the integrator to saturate. There are two main ways to solve this problem. One is to connect a switch in parallel with the feedback capacitor to periodically reset the feedback capacitor. The second is to add a dc feedback loop to extract the input low-frequency current. This allows the integrator to discharge continuously and avoid saturation.

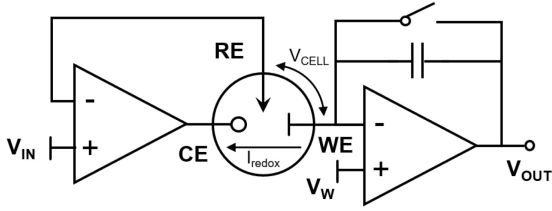


FIGURE 5. Capacitive feedback potentiostat.

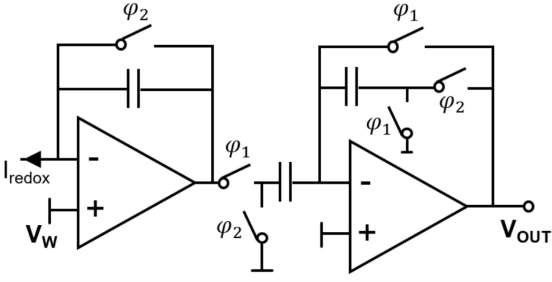


FIGURE 6. CDS technique (adapted from [60]).

As shown in Fig. 5, the switch-based structure cannot process the input signal when it is periodically reset. The dc offset noise usually causes problems such as saturation of the readout circuit. In order to eliminate the offset error, a correlated double sampling (CDS) circuit has been applied to the capacitive feedback readout circuit [60]. CDS circuits can also reduce $1/f$ noise. CDS removes low-frequency noise by sampling the input twice and recording the difference between the two samples. Fig. 6 shows an example CDS circuit where two sampling actions are implemented by a set of switches controlled by two clocks with opposite phases (ϕ_1 and ϕ_2).

The ability of this structure to handle small currents at high frequencies is limited. Dai et al. [61] proposed a self-timed switched capacitor reset network, as shown in Fig. 7. Two complementary control signals ϕ_1 and ϕ_2 are used alternately for C_{i1} and C_{d1} or C_{i2} and C_{d2} . So, there is always one capacitor in the working state and the other in the reset state. The system is self-timed and does not require an additional reset clock. The reset signal comes from the comparison of the output voltage of the integrator with the set threshold voltage. Both the integrator and the differentiator are reset in a charge-conserving manner, which minimizes the reset transient and recovery time. Furthermore, this configuration has inherent instant switching between voltage mode and frequency mode, which increases the dynamic range of the input current. The disadvantage is that at the moment of reset, the output voltage will have a small pulse due to mismatch.

Ferrari et al. [62] proposed a dc feedback loop based on the integrator-differentiator structure, as shown in Fig. 8. The dc gain of the dc feedback loop is

$$G_{\text{loop}} = -H(s) \frac{A}{1 + s(1 + A)C_i R_{dc}} \quad (4)$$

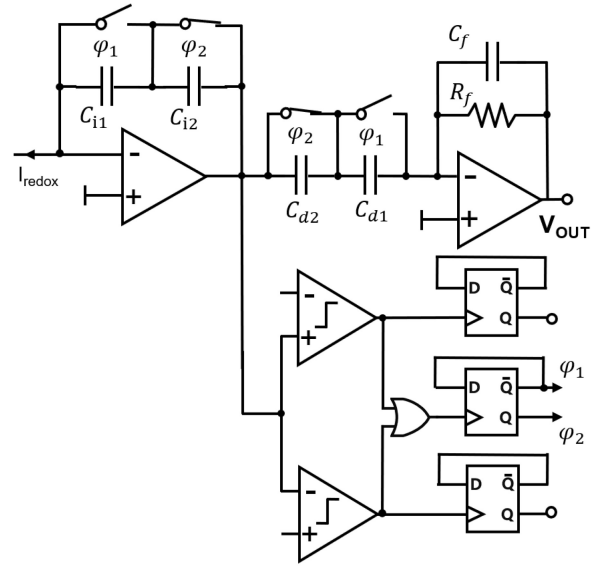


FIGURE 7. Self-timed capacitive feedback potentiostat [61].

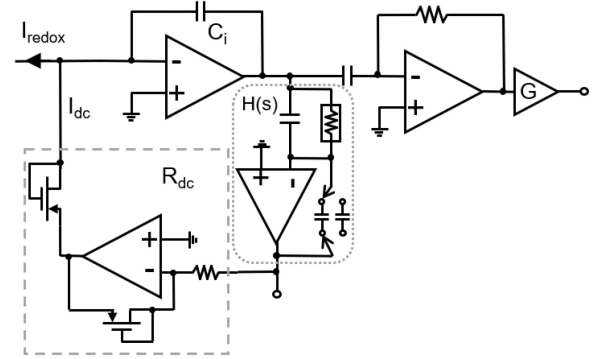


FIGURE 8. Capacitive Feedback potentiostat with dc feedback loop (adapted from [62]).

where A is the gain of the operational amplifier. At low frequency, the feedback is strong enough that I_{DC} flows into R_{dc} . At high frequency, the feedback fails and dc response of the output node is zero. Therefore, integrator saturation is avoided and the output dynamic range is increased. A large resistance on the order of $1 \text{ M}\Omega$ – $1 \text{ G}\Omega$ is required to ensure that the dominant pole of the dc feedback loop is small enough. Ferrari et al. [62] proposed an accurate current reducer based on a transconductor, as shown by the dashed box in Fig. 8. Since the dc feedback loop does not affect the signal of the desired frequency, the linearity of the resistance on this path is sufficient.

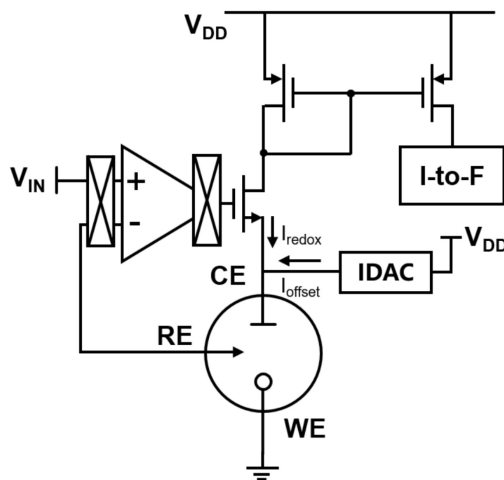
C. CURRENT-MIRROR BASED READOUT CIRCUITS

A CM-based potentiostat is another common current sensing structure, as shown in Fig. 9. This structure does not directly convert current to voltage. It mirrors the redox current and converts the current into a time or frequency signal through a modulator [13], [63]. However, the noise performance of the CM readout circuit is usually limited by the optional

TABLE 2. Performance summary of passive-electrode-based readout interface.

Ref.	Type	Volatge range	Current range	Resolution /Noise BW _{sig}	Power @Supply voltage	Technology	Sensing method	Target
[57]	R-TIA	-1.6-1.6 V	63 dB	N/A / N/A	15.8 mW@1.8 V	180 nm	CA/CV	Dopamine
[56]	R-TIA	-0.5-0.5 V	73 dB	10 nA / N/A	150 mW@ 6V	N/A	CV	Dopamine
[60]	C-TIA	-0.1-0.43 V	124 dB	6 pA / N/A	3 mW@5 V	0.6 μm	CV	N/A
[61]	C-TIA	N/A	155.1 dB	N/A / 204 fA _{rms} (in 100 Hz)	5.22 mW@1.8 V	180 nm	CA	Alamethicin
[65]	C-TIA	-0.4-1 V	67 dB	21.6 pA / 21.6 pA _{rms} (in 2.5 kHz)	12.1 μW@1.8 V	180 nm	CA/CV	Alamethicin
[8]	C-TIA	-0.5-0.8 V	156 dB	0.47 pA / 0.47 pA _{rms} (in 20 Hz)	9.3 mW@3.3 V	350 nm	CA/CV	Glucose
[66]	C-TIA	-0.4-1.3 V	98.6 dB	60 pA / 20 pA _{rms} (in 1 kHz)	3.1 μW@1.8 V	65 nm	FSCV	Dopamine
[67]	C-TIA	0.5-2 V	93 dB	0.28 pA / N/A	250 μW@2.5 V	250 nm	CV	DNA
[6]	CM	0.45-1.4 V	40.64 dB	71.8 nA / N/A	71.7 μW@1.8 V	180 nm	CA	Glucose
[63]	CM	-0.5-0 V	82.8 dB	N/A / 7.2 pA _{rms} (in 11.5 kHz)	21 μW@3.3 V	0.5μm	CV	N/A
[64]	CM	-0.5-0.5 V	108 dB	N/A / 41 pA _{rms} (0.1-20 Hz)	16 μW@1.2 V	180 nm	CA/CV	N/A
[4]	CM	-0.5-0.5 V	130 dB	2 pA / N/A	49 μW@1.2 V	180 nm	CA/CV/ FSCV/SWV	UA,CPR

* Dynamic range across multiple gain settings


FIGURE 9. Current-mirror-based readout circuits (adapted from [13]).

amplifier of the voltage bias circuit. Chopping techniques can be used to reduce bias circuit noise [4]. A current compensation circuit can be used to achieve bidirectional current sensing and output range extension [64]. In order to reduce the influence of the CM's channel length modulation effects, the large channel length or an enhancement CM topology can be used, such as a cascode or gain-boosted structure.

D. CASE STUDY OF PASSIVE-ELECTRODE-BASED READOUT INTERFACE

A summary of the performance of passive-electrode-based readout interfaces is shown in Table 2. For resistance feedback TIA(R-TIAs), since the large resistance is difficult to integrate on the chip, the thermal noise of the resistance limits the improvement in detection accuracy. An equivalent large resistance is achieved by using the pseudo-resistor, which can be used to detect small currents. However, as mentioned earlier, its PVT characteristics are not stable, and the high resistance makes it difficult to achieve a large bandwidth. Capacitive feedback TIAs (C-TIAs) can achieve low noise and large bandwidth, but requires additional circuits to avoid integrator saturation. The design of the TIA-based potentiostat is a compromise between the performance and

bandwidth. The CM potentiostat features low power consumption, small area, and a large dynamic range of detection current, making it suitable for multichannel applications. However, its bandwidth is relatively low and the sensitivity is relatively poor.

IV. ACTIVE ELECTRODES INTERFACE

In the passive electrode, the Faradaic current of the redox reaction is modified by the charging current of the double layer capacitor. As shown in (2), the amplitude of the redox current is proportional to the area of the WEs, what prevent scaling down the area.

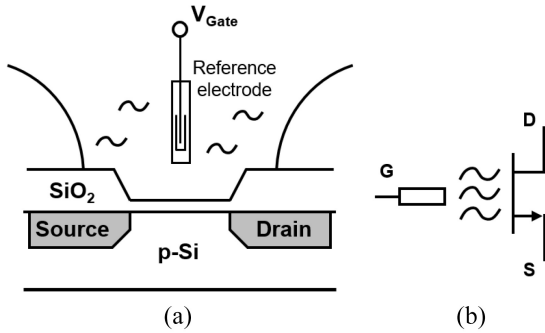
Active electrodes can change this issue using adsorption-based transducers. In the past 60 years, carrier-based ion-selective electrodes have been extensively studied and combined with the field-effect transistors. The response time of the ISFET is short. In addition, ISFETs can be fabricated using CMOS technology, opening up new opportunities for the development of compact system solution [68]. The first integrated multispecies electrodes, called extended gate chemically sensitive field effects (EGFETs), were introduced in 1983 [69]. Organic FETs (OFETs) represent a further development in materials. The easy functionalization of the electrodes is guaranteed by synthetic chemical modification. In the past decade, an OECT demonstrated its advantage using aqueous media. OECT uses hydrated, ion-permeable conducting polymers that change the OECT's conductivity through reversible ion exchange with electrolytes. High SNR is guaranteed due to its extremely high transconductance. In recent years, the main principle of OECT-based electrochemical sensors is to amplify redox voltage into current by utilizing the high transconductance.

A. ISFET AND READOUT CIRCUITS

The first ISFET was introduced by Bergveld in 1972. The schematic diagram and equivalent circuit of the ISFETs are as shown in Fig. 10. A typical ISFET consists of three terminals (source, drain, and gate) and an RE. Compared with three-electrode system, ISFETs exhibit a higher sensitivity with a smaller size. Only one RE is required to achieve a biochemical measurement. The working principle of ISFETs

TABLE 3. Materials and electrical parameters of recent ISFETs.

Ref.	Target	Materials	Detection limit	Sensitivity	Tech. CMOS	Readout method	Pixel size (μm^2)	Power(mW)
[70]	pH	Si_3N_4	0.03 pH	36.4 mV/pH	180 nm	CTIA	80×80	7.98
[71]	pH	DNA microarrays	N/A	49.7 mV/pH	180 nm	CTIA	Inner & Outer diameters: anodic rings: 26 & 36 cathodic rings: 58 & 62	N/A
[72]	pH, DNA	N/A	0.01 pH 0.5 mV	78.5 mV/pH	180 nm	N/A	58×62	N/A
[73]	pH	Si_3N_4	N/A	10 mV/pH	350 nm	Current-Mode Readout	44.9×33.5	4.02
[74]	Dopamine	SiNWs	1 pM	0.6 V/fM	350 nm	N/A	1×5	N/A
[75]	Cardiac Troponin I	AuNPs	N/A	1.77 Hz/pg-mL	180 nm	I-to-F	N/A	0.124
[76]	pH	Si_3N_4	N/A	11.9 mV/pH	350 nm	pH-to-time	37×31	7.5
[77]	pH	Si_3N_4	0.101 pH	1.03 $\mu A/pH$	350 nm	Current-Mode Readout	6.5×7.8	N/A
[78]	pH	Si_3N_4	0.08 pH	30.47 mV/pH	180 nm	Source follower	16×16	2.56
[79]	pH	TiN	0.015 pH	50 mV/pH	350 nm	N/A	8.5×8.5	N/A

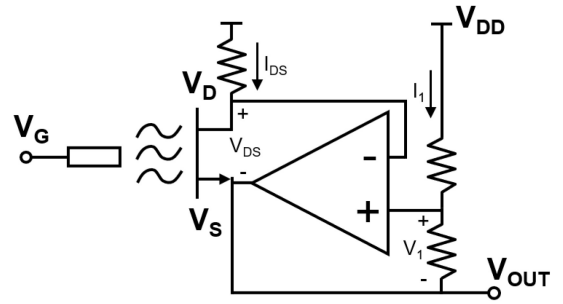

FIGURE 10. (a) Structure and (b) symbol of ISFET (adapted from [16]).

is based on the variation of the conduction of the channel adjusted by the potential on the RE. A positive bias applied on the RE will push the cations away from the gate surface, which results in a negative charge accumulation in the insulation layer. The charge redistribution on the gate will influence the threshold voltage (V_{th}) of ISFETs, leading to a change of the current I_{DS} . This process can be modulated by the surface reactions where the species of interest interact with the gate electrode.

The material studies on the ISFET most focus on the gate materials. High-k materials (including Si_3N_4 , Al_2O_3 , HfO_2 , ZrO_2 , etc.) are most common used as gate materials. By redesigning the structure of the device (e.g., extended gate structure, the Fin-gate structure, and stacking layers of gates), the performance of the ISFETs can be further improved. In addition, the modification of the gate electrode by introducing a microstructure on the gate or functionalizing with nanomaterials can improve the response time, sensitivity, and selectivity of the devices [80]. In addition, the functionalization of the ISFET gate gives more possibilities of the device to detect nonlabelled analytes, such as glucose, DNA, enzymes, protein biomarkers, and cell-related secretions or metabolism [80], [81].

For ISFETs, the threshold voltage V_{th} can be expressed as [82]

$$V_{th} = E_{ref} - \Psi + \chi^{sol} - \frac{\Phi_{Si}}{q} - \frac{Q_{ox} + Q_{ss} + Q_B}{C_{ox}} + 2\phi_f \quad (5)$$


FIGURE 11. Schematic representation of ISFET (adapted from [82]).

where E_{ref} is the constant potential of the reference electrode. Ψ is a chemical parameter, which is a function of the pH of the solution. χ^{sol} is the surface dipole potential of the solvent and therefore has a constant value. Φ_{Si} is the work function of silicon, Q_{ox} is due to the charge accumulated in the oxide, Q_{ss} is the charge at the oxide-silicon interface due to process defects, Q_B is the depletion region charge, and ϕ_f is the Fermi potential.

Table 3 summarizes the materials and properties of recent works on ISFETs and readout circuits. The readout circuit is critical for the drift and temperature issues of electrochemical sensing using ISFET. As shown in Fig. 11, a typical constant-voltage and constant-current (CVCC) test circuit generally biases the ISFET in the strong inversion region to ensure the linear relationship between I_d and V_{GS} . The I_d and V_{DS} of the ISFET are guaranteed to be fixed by I_1 and V_1 , and V_S will be read out as V_{out} when the pH changes. The change of source voltage V_S is proportional to the pH. CVCC circuits are immune to capacitive splitting caused by the passivation capacitors. However, the stability issues and difficulty in achieving inherent compensation limits the overall performance [16].

The current mode readout circuit has been widely used in recent years [83]. As shown in Fig. 12, with proper biasing, both MOS and ISFET in the circuit are biased in the weak inversion region. There is an exponential relationship between I_d and V_{GS} . Therefore, it can be deduced that the output current I_{out} is proportional to the H^+ concentration as

$$\frac{I_{out}}{I_{b1}} = e^{2\gamma/nU_T} e^{-2V_{ref}/U_T} [H^+] \quad (6)$$

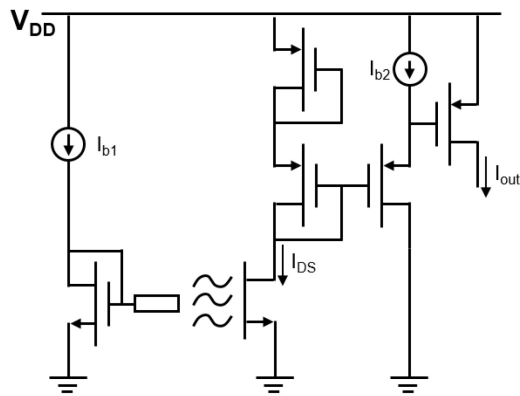


FIGURE 12. Current-mode readout of ISFET (adapted from [16]).

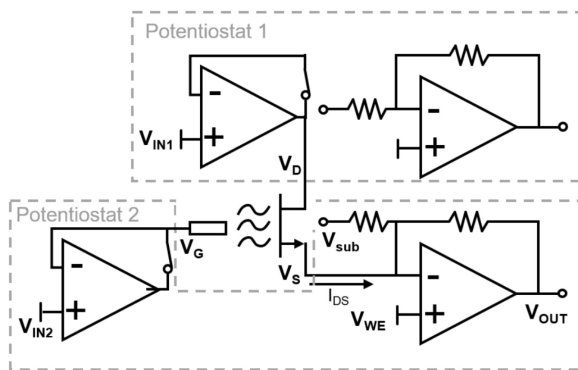


FIGURE 13. Reconfigurable platform for ISFET (adapted from [84]).

where n is the subthreshold slope parameter. γ is a grouping of pH-independent chemical potentials and U_T is the thermal voltage [83].

A combination of potentiostats which is used for three-electrode systems can also be multiplexed with ISFETs as shown in Fig. 13 [84]. The voltage V_D is biased by the potentiostat 1. The voltages V_G and V_S are biased by potentiostat 2. The current I_{DS} is readout by potentiostat 2.

B. OECT AND READOUT CIRCUITS

The first OEET was reported by White et al. [101] in the mid-1980s. As shown in Fig. 14, metal electrodes (a source, a drain, and a gate electrode) and an organic semiconductor film lying between the source and drain electrodes represent a typical structure of OEETs. Different from conventional FETs, OEETs rely on ions injection or extraction from the electrolyte into the organic films, leading to changes of its doping state and conductivity.

As a typical material for OECTs, the reversible doping process of conducting polymer poly(3, 4-ethylenedioxythiophene) doped with poly(styrene sulfonate) (PEDOT:PSS) can be described as [102]

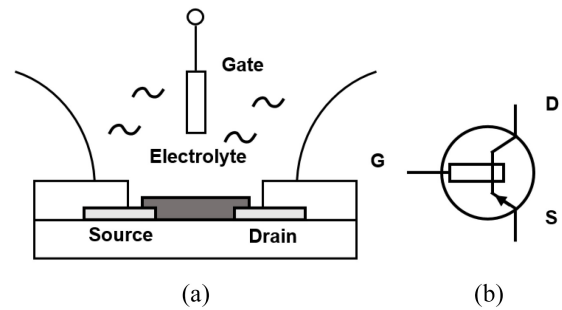
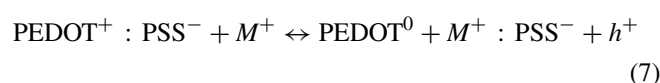


FIGURE 14. (a) Structure and (b) symbol of OECT.

OECTs based on PEDOT:PSS operate in a depletion mode. During the operation, a positive gate bias pushes positive cations (M^+) from the electrolyte into the PEDOT:PSS layer and the hole density in the PEDOT+ is reduced followed by the decrease of the channel current [103]. Compared with ISFET in which the physical thickness of the channel does not tune the performance of the device, volumetric gating gives OECTs a much larger transconductance than that of ISFETs up to a certain frequency range (up to kilohertz) [104]. When serving as an electrochemical sensor, the redox reactions on the gate electrode cause an increase in the potential at the electrolyte/channel interface which pumps extra positive cations (M^+) from the electrolyte into the PEDOT:PSS channel [105]. The whole process can be described by the following equation based on Bernard's model [106]:

$$\Delta V_{g-\text{eff}} \approx 2.30(1 + \gamma) \frac{\kappa T}{2q} \log(\text{analyte}) + C \quad (8)$$

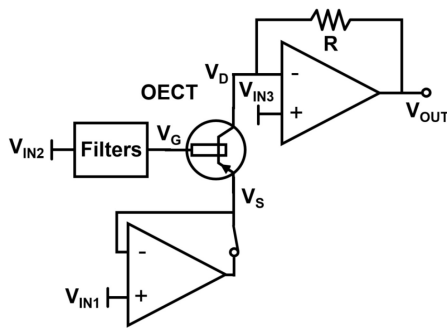
where $\Delta V_{g-\text{eff}}$ is the change of the effective gate voltage generated by the redox reactions; γ is the ratio between the electrolyte/channel capacitance and the gate/electrolyte capacitance; k is the Boltzmann constant, T is the absolute temperature, q is the charge of an electron, and (analyte) is the concentration of species of interest; and C is a constant.

Table 4 summarizes active materials and key electrical parameters of recent works of OECTs. Apart from PEDOT:PSS, other conjugated polymers can also be used to fabricate the channel of OECTs. These conjugated polymers, as well as PEDOT:PSS, all exhibit attractive electrical properties with simple fabrication process. For typical OECTs, the potential range of both the drain-source voltage (V_{ds}) and the gate-source voltage (V_{gs}) is -1 to $+1$ V. The drain-source current (I_{ds}) is around few mA to dozens of nA. Generally, OECTs exhibit a transconductance up to dozens of mS during operation at low frequencies [104].

OECT has been used for various electrochemical detections that can be performed using traditional three electrodes configuration [22], [23], [24]. The readout circuits of the three-electrode systems are also being used for OECTs. This requires adding a voltage bias and properly adjusting the range of the readout current. As shown in Fig. 15, Tian et al. [24] used DAC₂ to configure the voltage V_g .

TABLE 4. Materials and electrical parameters of recent OEECTs.

Ref.	Active material	$V_{gs, gm(max)}$ (V)	V_{ds} (V)	$g_{m(max)}$ (mS)	I_{on}/I_{off}	V_T (V)	τ (ms)
[85]	p(gPyDPP-MeOT2)	-0.7	-0.4	1.4	10^5	N/A	770
[86]	p(gDPP-T2)	-0.8	-0.6	6.3	10^5	-0.52	N/A
[87]	PIBET-AO	<-0.6	-0.6	14	$\sim 10^4$	0.44	590
[88]	g2T-T	N/A	-0.4	7.9	10^5	N/A	N/A
[89]	p(g3T2-T)	-0.6	-0.6	3.0	10^5	-0.18	0.91
[90]	p(g2T-TT)	-0.1	-0.4	~ 20	10^5	0.03	20
[91]	p(g2T-TT)	N/A	-0.6	5.4	10^5	>0.7	N/A
[92]	p(g2T-T)	-0.5	-0.6	4.2	10^4	<0.07	N/A
[93]	PEDOT:PSS	-0.15	-0.1	48.7	10^3	0.36	5.7
[94]	PEDOT:PSS	0.5	-0.6	32.3	10^6	>0.4	0.317
[95]	PEDOT:PSS	-0.5	-0.6	52.74	N/A	N/A	0.0029
[96]	PEDOT:PSS	-0.4	-0.8	~ 1.0	10^3	>0.7	N/A
[97]	PEDOT:PSS	~ -0.1	-0.5	~ 13.0	10^4	0.4	0.046
[98]	PEDOT:PSS	0.2	-0.6	4.02	N/A	N/A	0.102
[99]	PEDOT:PSS	1.0	-0.2	~ 2	$\sim 10^5$	N/A	N/A
[100]	PEDOT:PSS	0	-0.6	19	$\sim 10^2$	N/A	N/A

**FIGURE 15.** Readout circuit for OEECT in [24].

Due to the high SNR of OEECT, the circuit design has not been very challenging yet. However, the nonlinearity of the readout current and the power consumption caused by the high-current I_{DS} are worth improving. Similar to ISFETs, OEECTs will also develop toward miniaturized and arrayed applications, which also require adapted readout circuits.

V. CONCLUSION

For decades, electrochemical detection based on redox reactions has been widely used. This article analyzed the challenges in the electrochemical interface and summarized the response time required for common analytes and the corresponding concentration ranges for different electrode materials, which help the design of readout circuits to achieve tradeoffs between accuracy, bandwidth, and power consumption. In recent years, the development of active electrodes has solved many difficulties of passive electrodes in the improvement of temporal and spatial resolution. This article also reviewed and analyzed the key performances of ISFETs and OEECTs published in recent years. The readout circuits of ISFETs require multichannel and adaptive nonideal compensation. There is no published OEECT readout circuit, but it can be expected that the circuit needs to be optimized for power consumption while maintaining a high signal-to-noise ratio.

REFERENCES

- [1] J. Wang, "Electrochemical biosensors: Towards point-of-care cancer diagnostics," *Biosensors Bioelectron.*, vol. 21, no. 10, pp. 1887–1892, 2006.
- [2] R. Li et al., "A flexible and physically transient electrochemical sensor for real-time wireless nitric oxide monitoring," *Nat. Commun.*, vol. 11, no. 1, pp. 1–11, 2020.
- [3] J. Dieffenderfer, M. Wilkins, C. Hood, E. Beppler, M. A. Daniele, and A. Bozkurt, "Towards a sweat-based wireless and wearable electrochemical sensor," in *Proc. IEEE Sensors*, 2016, pp. 1–3.
- [4] S.-Y. Lu et al., "18.4 a wireless multimodality system-on-a-chip with time-based resolution scaling technique for chronic wound monitoring," in *Proc. IEEE Int. Solid-State Circuits Conf. (ISSCC)*, vol. 64, 2021, pp. 282–284.
- [5] J. Kim and H. Ko, "A 1.2 V low-power CMOS chopper-stabilized analog front-end IC for glucose monitoring," *IEEE Sensors J.*, vol. 16, no. 17, pp. 6517–6518, Sep. 2016.
- [6] K. A. A. Mamun, S. K. Islam, D. K. Hensley, and N. McFarlane, "A glucose biosensor using CMOS potentiostat and vertically aligned carbon nanofibers," *IEEE Trans. Biomed. Circuits Syst.*, vol. 10, no. 4, pp. 807–816, Aug. 2016.
- [7] S. Mross, P. Fürst, S. Pierrat, T. Zimmermann, H. Vogt, and M. Kraft, "Enzyme sensor with Polydimethylsiloxane membrane and CMOS potentiostat for wide-range glucose measurements," *IEEE Sensors J.*, vol. 15, no. 12, pp. 7096–7104, Dec. 2015.
- [8] S. S. Ghoreishizadeh, I. Taurino, G. D. Micheli, S. Carrara, and P. Georgiou, "A differential electrochemical readout ASIC with heterogeneous integration of bio-nano sensors for amperometric sensing," *IEEE Trans. Biomed. Circuits Syst.*, vol. 11, no. 5, pp. 1148–1159, Oct. 2017.
- [9] S. Y. Lu et al., "A review of CMOS electrochemical readout interface designs for biomedical assays," *IEEE Sensors J.*, vol. 21, no. 11, pp. 12469–12483, Jun. 2021.
- [10] H. Li, X. Liu, L. Li, X. Mu, R. Genov, and A. Mason, "CMOS electrochemical instrumentation for biosensor microsystems: A review," *Sensors*, vol. 17, no. 1, p. 74, 2017.
- [11] R. J. Reay, S. P. Kounaves, and G. T. Kovacs, "An integrated CMOS potentiostat for miniaturized electroanalytical instrumentation," in *Proc. IEEE Int. Solid-State Circuits Conf. (ISSCC)*, 1994, pp. 162–163.
- [12] R. F. B. Turner, D. J. Harrison, and H. P. Baltes, "A CMOS potentiostat for amperometric chemical sensors," *IEEE J. Solid-State Circuits*, vol. SSC-22, no. 3, pp. 473–478, Jun. 1987.
- [13] M. M. Ahmadi and G. A. Jullien, "Current-mirror-based potentiostats for three-electrode amperometric electrochemical sensors," *IEEE Trans. Circuits Syst. I, Reg. Papers*, vol. 56, no. 7, pp. 1339–1348, Jul. 2009.
- [14] Y. Ma, R. Li, J. Lei, M. Zhang, and L. Yin, "Design of a wireless compact implantable electrochemical biosensor system for health monitoring application," in *Proc. IEEE Int. Conf. Integr. Circuits Technol. Appl. (ICTA)*, 2020, pp. 137–138.

- [15] C. Xie, Y. Ma, Z. Tang, and M. Zhang, "Design of a 68 dB input dynamic range Potentiostat for electrochemical biosensing," in *Proc. IEEE 6th Int. Conf. Integr. Circuits Microsyst. (ICICM)*, 2021, pp. 426–429.
- [16] N. Moser, T. S. Lande, C. Toumazou, and P. Georgiou, "ISFETs in CMOS and emergent trends in instrumentation: A review," *IEEE Sensors J.*, vol. 16, no. 17, pp. 6496–6514, Sep. 2016.
- [17] P. Georgiou and C. Toumazou, "An adaptive ISFET chemical imager chip," in *Proc. IEEE Int. Symp. Circuits Syst.*, 2008, pp. 2078–2081.
- [18] B. Nemeth, M. S. Piechocinski, and D. R. Cumming, "High-resolution real-time ion-camera system using a CMOS-based chemical sensor array for proton imaging," *Sensors Actuators B Chem.*, vols. 171–172, pp. 747–752, Aug./Sep. 2012.
- [19] J. M. Rothberg et al., "An integrated semiconductor device enabling non-optical genome sequencing," *Nature*, vol. 475, no. 7356, pp. 348–352, 2011.
- [20] D. M. Garner et al., "A multichannel DNA SoC for rapid point-of-care gene detection," in *Proc. IEEE Int. Solid-State Circuits Conf. (ISSCC)*, 2010, pp. 492–493.
- [21] X. Huang, F. Wang, J. Guo, M. Yan, H. Yu, and K. S. Yeo, "A 64×64 1200fps CMOS ion-image sensor with suppressed fixed-pattern-noise for accurate high-throughput DNA sequencing," in *IEEE Symp. VLSI Circuits Dig. Tech. Papers*, 2014, pp. 1–2.
- [22] P. Lin, X. Luo, I.-M. Hsing, and F. Yan, "Organic electrochemical transistors integrated in flexible microfluidic systems and used for label-free DNA sensing," *Adv. Mater.*, vol. 23, no. 35, pp. 4035–4040, 2011.
- [23] E. Bihar, Y. Deng, T. Miyake, M. Saadaoui, G. G. Malliaras, and M. Rolandi, "A disposable paper breathalyzer with an alcohol sensing organic electrochemical transistor," *Sci. Rep.*, vol. 6, no. 1, pp. 1–6, 2016.
- [24] X. Tian et al., "Pushing OECTs toward wearable: Development of a miniaturized analytical control unit for wireless device characterization," *Anal. Chem.*, vol. 94, no. 16, pp. 6156–6162, 2022.
- [25] P. Malik, R. Gupta, V. Malik, and R. K. Ameta, "Emerging nanomaterials for improved biosensing," *Meas. Sensors*, vol. 16, Aug. 2021, Art. no. 100050.
- [26] M. A. Deshmukh, B.-C. Kang, and T.-J. Ha, "Non-enzymatic electrochemical glucose sensors based on polyaniline/reduced-graphene-oxide nanocomposites functionalized with silver nanoparticles," *J. Mater. Chem. C*, vol. 8, no. 15, pp. 5112–5123, 2020.
- [27] D.-H. Kim, R. Ghaffari, N. Lu, and J. A. Rogers, "Flexible and stretchable electronics for biointegrated devices," *Annu. Rev. Biomed. Eng.*, vol. 14, no. 1, pp. 113–128, 2012.
- [28] A. J. Bard, L. R. Faulkner, and H. S. White, *Electrochemical Methods: Fundamentals and Applications*. Hoboken, NJ, USA: Wiley, 2022.
- [29] F. Scholz, "Voltammetric techniques of analysis: The essentials," *ChemTexts*, vol. 1, no. 4, pp. 1–24, 2015.
- [30] A. Amine and H. A. Mohammadi, *Reference Module in Chemistry, Molecular Sciences and Chemical Engineering*. Amsterdam, The Netherlands: Elsevier BV, 2018.
- [31] E. O. Polat et al., "Transducer technologies for biosensors and their wearable applications," *Biosensors*, vol. 12, no. 6, p. 385, 2022.
- [32] D. Grieshaber, R. MacKenzie, J. Vörös, and E. Reimhult, "Electrochemical biosensors-sensor principles and architectures," *Sensors*, vol. 8, no. 3, pp. 1400–1458, 2008.
- [33] N. Elgrishi, K. J. Rountree, B. D. McCarthy, E. S. Rountree, T. T. Eisenhart, and J. L. Dempsey, "A practical beginner's guide to cyclic voltammetry," *J. Chem. Educ.*, vol. 95, no. 2, pp. 197–206, 2018.
- [34] F. Crespi, "Differential pulse Voltammetry: Evolution of an *in vivo* methodology and new chemical entries, a short review," *J. New Develop. Chem.*, vol. 2, pp. 20–28, Apr. 2020.
- [35] V. Mirceski, R. Gulaboski, M. Lovric, I. Bogeski, R. Kappl, and M. Hoth, "Square-wave voltammetry: A review on the recent progress," *Electroanalysis*, vol. 25, no. 11, pp. 2411–2422, 2013.
- [36] Q. He et al., "A promising sensing platform toward dopamine using MnO₂ nanowires/electro-reduced graphene oxide composites," *Electrochimica Acta*, vol. 296, pp. 683–692, Feb. 2019.
- [37] Q. Huang, X. Lin, L. Tong, and Q.-X. Tong, "Graphene quantum dots/multiwalled carbon nanotubes composite-based electrochemical sensor for detecting dopamine release from living cells," *ACS Sustain. Chem. Eng.*, vol. 8, no. 3, pp. 1644–1650, 2020.
- [38] L. Ma, Q. Zhang, C. Wu, Y. Zhang, and L. Zeng, "PtNi bimetallic nanoparticles loaded MoS₂ nanosheets: Preparation and electrochemical sensing application for the detection of dopamine and uric acid," *Analytica Chimica Acta*, vol. 1055, pp. 17–25, May 2019.
- [39] J. Yang, Y. Hu, and Y. Li, "Molecularly imprinted polymer-decorated signal on-off ratiometric electrochemical sensor for selective and robust dopamine detection," *Biosensors Bioelectron.*, vol. 135, pp. 224–230, Jun. 2019.
- [40] P. Shaikhavali et al., "A simple sonochemical assisted synthesis of nanocomposite (ZnO/MWCNTs) for electrochemical sensing of epinephrine in human serum and pharmaceutical formulation," *Colloids Surfaces A Physicochem. Eng. Aspects*, vol. 584, Jan. 2020, Art. no. 124038.
- [41] A. Fajardo, D. Tapia, J. Pizarro, R. Segura, and P. Jara, "Determination of norepinephrine using a glassy carbon electrode modified with graphene quantum dots and gold nanoparticles by square wave stripping voltammetry," *J. Appl. Electrochem.*, vol. 49, no. 4, pp. 423–432, 2019.
- [42] G. Gumilar et al., "General synthesis of hierarchical sheet/plate-like M-BDC (M = Cu, Mn, Ni, and Zr) metal-organic frameworks for electrochemical non-enzymatic glucose sensing," *Chem. Sci.*, vol. 11, no. 14, pp. 3644–3655, 2020.
- [43] W.-C. Lee et al., "Comparison of enzymatic and non-enzymatic glucose sensors based on hierarchical Au-Ni alloy with conductive polymer," *Biosensors Bioelectron.*, vol. 130, pp. 48–54, Apr. 2019.
- [44] C. W. Bae et al., "Fully stretchable capillary microfluidics-integrated nanoporous gold electrochemical sensor for wearable continuous glucose monitoring," *ACS Appl. Mater. Interfaces*, vol. 11, no. 16, pp. 14567–14575, 2019.
- [45] L. Wu, Z. Lu, and J. Ye, "Enzyme-free glucose sensor based on layer-by-layer electrodeposition of multilayer films of multi-walled carbon nanotubes and Cu-based metal framework modified glassy carbon electrode," *Biosensors Bioelectron.*, vol. 135, pp. 45–49, Jun. 2019.
- [46] T. Liu et al., "Silver nanoparticle-functionalized 3D flower-like copper (II)-porphyrin framework nanocomposites as signal enhancers for fabricating a sensitive glutathione electrochemical sensor," *Sensors Actuators B Chem.*, vol. 342, Sep. 2021, Art. no. 130047.
- [47] L. Chuang et al., "Flexible nitrogen dioxide gas sensor based on reduced graphene oxide sensing material using silver nanowire electrode," *Acta Physica Sinica*, vol. 69, no. 5, p. 10, 2020.
- [48] S. Shinde, C.-Y. Jiang, C.-X. Zheng, Y.-Z. Wang, K.-M. Lin, and P. M. Koinkar, "Room-temperature and flexible PEDOT: PSS-WO₃ gas sensor for nitrogen dioxide detection," *Modern Phys. Lett. B*, vol. 33, no. 14n15, 2019, Art. no. 1940013.
- [49] A. Aziz et al., "Boosting electrocatalytic activity of carbon fiber@fusiform-like copper-nickel LDHs: Sensing of nitrate as biomarker for NOB detection," *J. Hazardous Mater.*, vol. 422, Jan. 2022, Art. no. 126907.
- [50] J. Baranwal, B. Barse, G. Gatto, G. Broncova, and A. Kumar, "Electrochemical sensors and their applications: A review," *Chemosensors*, vol. 10, no. 9, p. 363, 2022.
- [51] V. Trovato et al., "A review of stimuli-responsive smart materials for wearable technology in Healthcare: Retrospective, perspective, and prospective," *Molecules*, vol. 27, no. 17, p. 5709, 2022.
- [52] A. Fethi, "Novel materials for electrochemical sensing platforms," *Sensors Int.*, vol. 1, Jan. 2020, Art. no. 100035.
- [53] D. H. Ho, Y. Y. Choi, S. B. Jo, J.-M. Myoung, and J. H. Cho, "Sensing with MXenes: Progress and prospects," *Adv. Mater.*, vol. 33, no. 47, 2021, Art. no. 2005846.
- [54] J. Wang, "Modified electrodes for electrochemical sensors," *Electroanalysis*, vol. 3, nos. 4–5, pp. 255–259, 1991.
- [55] V. S. Reddy et al., "Recent advancement in Biofluid-based glucose sensors using invasive, minimally invasive, and non-invasive technologies: A review," *Nanomaterials*, vol. 12, no. 7, p. 1082, 2022.
- [56] E. Ghodsevali, B. Gosselin, M. Boukadoum, and A. Miled, "High accuracy and sensitivity differential potentiostat with amplifier-based error cancellation feedback loop," in *Proc. IEEE Biomed. Circuits Syst. Conf. (BioCAS)*, 2015, pp. 1–4.
- [57] S. M. Martin, F. H. Gebara, T. D. Strong, and R. B. Brown, "A fully differential potentiostat," *IEEE Sensors J.*, vol. 9, no. 2, pp. 135–142, Feb. 2009.

- [58] D. Djekic, G. Fantner, K. Lips, M. Ortmanns, and J. Anders, "A 0% THD, 1-M ω to 1-G ω tunable, temperature-compensated transimpedance amplifier using a multi-element pseudo-resistor," *IEEE J. Solid-State Circuits*, vol. 53, no. 7, pp. 1913–1923, Jul. 2018.
- [59] R. G. Kakerow, H. Kappert, E. Spiegel, and Y. Manoli, "Low-power single-chip CMOS potentiostat," in *Proc. IEEE Int. Solid-State Sensors Actuators Conf. Transducers*, vol. 1, 1995, pp. 142–145.
- [60] C. Yang, Y. Huang, B. L. Hassler, R. M. Worden, and A. J. Mason, "Amperometric electrochemical microsystem for a miniaturized protein biosensor array," *IEEE Trans. Biomed. Circuits Syst.*, vol. 3, no. 3, pp. 160–168, Jun. 2009.
- [61] S. Dai, R. T. Perera, Z. Yang, and J. K. Rosenstein, "A 155-dB dynamic range current measurement front end for electrochemical biosensing," *IEEE Trans. Biomed. Circuits Syst.*, vol. 10, no. 5, pp. 935–944, Oct. 2016.
- [62] G. Ferrari, F. Gozzini, A. Molari, and M. Sampietro, "Transimpedance amplifier for high sensitivity current measurements on nanodevices," *IEEE J. Solid-State Circuits*, vol. 44, no. 5, pp. 1609–1616, May 2009.
- [63] H. Li, S. Parsnejad, E. Ashoori, C. Thompson, E. K. Purcell, and A. J. Mason, "Ultracompact microwatt CMOS current readout with picoampere noise and kilohertz bandwidth for biosensor arrays," *IEEE Trans. Biomed. Circuits Syst.*, vol. 12, no. 1, pp. 35–46, Feb. 2018.
- [64] Y. C. Chen, S. Y. Lu, and Y. T. Liao, "A microwatt dual-mode electrochemical sensing current readout with current-reducer ramp waveform generation," *IEEE Trans. Biomed. Circuits Syst.*, vol. 13, no. 6, pp. 1163–1174, Dec. 2019.
- [65] J. Guo, W. Ng, J. Yuan, S. Li, and M. Chan, "A 200-channel area-power-efficient chemical and electrical dual-mode acquisition IC for the study of Neurodegenerative diseases," *IEEE Trans. Biomed. Circuits Syst.*, vol. 10, no. 3, pp. 567–578, Jun. 2016.
- [66] B. Nasri et al., "Hybrid CMOS-graphene sensor array for subsecond dopamine detection," *IEEE Trans. Biomed. Circuits Syst.*, vol. 11, no. 6, pp. 1192–1203, Dec. 2017.
- [67] A. Manickam et al., "A CMOS electrochemical biochip with 32×32 three-electrode voltammetry pixels," *IEEE J. Solid-State Circuits*, vol. 54, no. 11, pp. 2980–2990, Nov. 2019.
- [68] L. Ravezzi and P. Conci, "ISFET sensor coupled with CMOS read-out circuit microsystem," *Electron. Lett.*, vol. 34, no. 23, pp. 2234–2235, 1998.
- [69] J. van der Spiegel, I. Lauks, P. Chan, and D. Babic, "The extended gate chemically sensitive field effect transistor as multi-species microprobe," *Sensors Actuators*, vol. 4, pp. 291–298, Jan. 1983.
- [70] M. Duan, X. Zhong, X. Zhao, O. M. El-Agnaf, Y.-K. Lee, and A. Bermak, "An optical and temperature assisted CMOS ISFET sensor array for robust E. Coli detection," *IEEE Trans. Biomed. Circuits Syst.*, vol. 15, no. 3, pp. 497–508, Jun. 2021.
- [71] H. S. Jung et al., "CMOS electrochemical pH localizer-imager," *Sci. Adv.*, vol. 8, no. 30, 2022, Art. no. eabm6815.
- [72] P. Sun, Y. Cong, M. Xu, H. Si, D. Zhao, and D. Wu, "An ISFET microarray sensor system for detecting the DNA base pairing," *Micromachines*, vol. 12, no. 7, p. 731, 2021.
- [73] M. S. Baghini, A. Vilouras, and R. Dahiya, "Ultra-thin chips with ISFET array for continuous monitoring of body fluids pH," *IEEE Trans. Biomed. Circuits Syst.*, vol. 15, no. 6, pp. 1174–1185, Dec. 2021.
- [74] V. Sessi et al., "Multisite dopamine sensing with Femtomolar resolution using a CMOS enabled Aptasensor chip," *Front. Neurosci.*, vol. 16, Jun. 2022, Art. no. 875656.
- [75] S.-S. Shan et al., "A two-electrode, double-pulsed sensor readout circuit for cardiac Troponin I measurement," *IEEE Trans. Biomed. Circuits Syst.*, vol. 14, no. 6, pp. 1362–1370, Dec. 2020.
- [76] N. Moser, J. Rodriguez-Manzano, T. S. Lande, and P. Georgiou, "A scalable ISFET sensing and memory array with sensor auto-calibration for on-chip real-time DNA detection," *IEEE Trans. Biomed. Circuits Syst.*, vol. 12, no. 2, pp. 390–401, Apr. 2018.
- [77] N. Miskourides, L.-S. Yu, J. Rodriguez-Manzano, and P. Georgiou, "A 12.8 k current-mode velocity-saturation ISFET array for on-chip real-time DNA detection," *IEEE Trans. Biomed. Circuits Syst.*, vol. 12, no. 5, pp. 1202–1214, Oct. 2018.
- [78] J. Zeng et al., "A Location imaging platform for spatio-temporal characterisation of ion-selective membranes," *IEEE Trans. Biomed. Circuits Syst.*, vol. 16, no. 4, pp. 545–556, Oct. 2022.
- [79] N.-Y. Teng and C.-T. Lin, "CMOS ISFETs with 3D-truncated sensing structure resistant to scaling attenuation and trapped charge-induced offset," *IEEE Sensors J.*, vol. 21, no. 24, pp. 27282–27289, Dec. 2021.
- [80] S. Cao et al., "ISFET-based sensors for (bio) chemical applications: A review," *Electrochem. Sci. Adv.*, Mar. 2022, Art. no. e2100207.
- [81] Y. Su and W. Hsu, "Review field effect transistor biosensing: Devices and clinical applications," *ECS J. Solid-State Sci. Technol.*, vol. 7, Jun. 2018, Art. no. Q3196.
- [82] P. Bergveld, "Thirty years of ISFETOLOGY: What happened in the past 30 years and what may happen in the next 30 years," *Sensors Actuators B Chem.*, vol. 88, no. 1, pp. 1–20, 2003.
- [83] L. M. Shepherd and C. Toumazou, "A biochemical translinear principle with weak inversion ISFETs," *IEEE Trans. Circuits Syst. I, Reg. Papers*, vol. 52, no. 12, pp. 2614–2619, Dec. 2005.
- [84] I. Lee et al., "A reconfigurable and portable highly sensitive biosensor platform for ISFET and enzyme-based sensors," *IEEE Sensors J.*, vol. 16, no. 11, pp. 4443–4451, Jun. 2016.
- [85] A. Giovannitti et al., "Energetic control of redox-active polymers toward safe organic bioelectronic materials," *Adv. Mater.*, vol. 32, no. 16, 2020, Art. no. 1908047.
- [86] M. Moser et al., "Polaron delocalization in Donor–Acceptor polymers and its impact on organic electrochemical transistor performance," *Angewandte Chemie*, vol. 60, no. 14, pp. 7777–7785, 2021.
- [87] Y. Wang et al., "Hybrid Alkyl–Ethylene glycol side chains enhance substrate adhesion and operational stability in accumulation mode organic electrochemical transistors," *Chem. Mater.*, vol. 31, no. 23, pp. 9797–9806, 2019.
- [88] C. B. Nielsen et al., "Molecular design of semiconducting polymers for high-performance organic electrochemical transistors," *J. Amer. Chem. Soc.*, vol. 138, no. 32, pp. 10252–10259, 2016.
- [89] M. Moser et al., "Ethylene glycol-based side chain length engineering in polythiophenes and its impact on organic electrochemical transistor performance," *Chem. Mater.*, vol. 32, no. 15, pp. 6618–6628, 2020.
- [90] C. Cendra et al., "Role of the anion on the transport and structure of organic mixed conductors," *Adv. Funct. Mater.*, vol. 29, no. 5, 2019, Art. no. 1807034.
- [91] A. Giovannitti et al., "Controlling the mode of operation of organic transistors through side-chain engineering," *Proc. Nat. Acad. Sci. USA*, vol. 113, no. 43, pp. 12017–12022, 2016.
- [92] Y. Dai et al., "Stretchable redox-active semiconducting polymers for high-performance organic electrochemical transistors," *Adv. Mater.*, vol. 34, no. 23, 2022, Art. no. 2201178.
- [93] J. Ko, X. Wu, A. Surendran, B. T. Muhammad, and W. L. Leong, "Self-healable organic electrochemical transistor with high transconductance, fast response, and long-term stability," *ACS Appl. Mater. Interfaces*, vol. 12, no. 30, pp. 33979–33988, 2020.
- [94] G. D. Spyropoulos, J. N. Gelinas, and D. Khodagholy, "Internal ion-gated organic electrochemical transistor: A building block for integrated bioelectronics," *Sci. Adv.*, vol. 5, no. 2, 2019, Art. no. eaau7378.
- [95] C. Cea, G. D. Spyropoulos, P. Jastrzebska-Perfect, J. J. Ferrero, J. N. Gelinas, and D. Khodagholy, "Enhancement-mode ion-based transistor as a comprehensive interface and real-time processing unit for *in vivo* electrophysiology," *Nat. Mater.*, vol. 19, no. 6, pp. 679–686, 2020.
- [96] Y. Kim et al., "Strain-engineering induced anisotropic crystallite orientation and maximized carrier mobility for high-performance microfiber-based organic bioelectronic devices," *Adv. Mater.*, vol. 33, no. 10, 2021, Art. no. 2007550.
- [97] T. Li et al., "Biocompatible ionic liquids in high-performing organic electrochemical transistors for ion detection and electrophysiological monitoring," *ACS Nano*, vol. 16, no. 8, pp. 12049–12060, 2022.
- [98] D. Khodagholy et al., "High transconductance organic electrochemical transistors," *Nat. Commun.*, vol. 4, no. 1, pp. 1–6, 2013.
- [99] Y. Deng et al., "A flexible and highly sensitive organic electrochemical transistor-based biosensor for continuous and wireless nitric oxide detection," *Proc. Nat. Acad. Sci. USA*, vol. 119, no. 34, 2022, Art. no. e2208060119.
- [100] S.-M. Kim et al., "Influence of PEDOT: PSS crystallinity and composition on electrochemical transistor performance and long-term stability," *Nat. Commun.*, vol. 9, no. 1, pp. 1–9, 2018.

- [101] H. S. White, G. P. Kittlesen, and M. S. Wrighton, "Chemical derivatization of an array of three gold microelectrodes with polypyrrole: Fabrication of a molecule-based transistor," *J. Amer. Chem. Soc.*, vol. 106, no. 18, pp. 5375–5377, 1984.
- [102] J. T. Friedlein, R. R. McLeod, and J. Rivnay, "Device physics of organic electrochemical transistors," *Organ. Electron.*, vol. 63, pp. 398–414, Dec. 2018.
- [103] L. Bai, C. G. Elósegui, W. Li, P. Yu, J. Fei, and L. Mao, "Biological applications of organic electrochemical transistors: Electrochemical biosensors and electrophysiology recording," *Front. Chem.*, vol. 7, p. 313, May 2019.
- [104] J. Rivnay, S. Inal, A. Salleo, R. M. Owens, M. Berggren, and G. G. Malliaras, "Organic electrochemical transistors," *Nat. Rev. Mater.*, vol. 3, no. 2, pp. 1–14, 2018.
- [105] D. A. Bernards, D. J. Macaya, M. Nikolou, J. A. DeFranco, S. Takamatsu, and G. G. Malliaras, "Enzymatic sensing with organic electrochemical transistors," *J. Mater. Chem.*, vol. 18, no. 1, pp. 116–120, 2008.
- [106] K. Xie et al., "Organic electrochemical transistor arrays for real-time mapping of evoked neurotransmitter release *in vivo*," *Elife*, vol. 9, Feb. 2020, Art. no. e50345.



BINGJING ZHANG is currently pursuing the B.S. degree with the Department of Electronic and Engineering, Tsinghua University, Beijing, China.

She is currently working on interface circuit design for electrochemical sensors.



BOYU SHEN is currently pursuing the B.S. degree with the School of Materials Science and Engineering, Tsinghua University, Beijing, China.

His current research interests focus on electrochemical biosensors.



YUAN MA received the B.S. degree in electronic engineering from Tsinghua University, Beijing, China, in 2019, where she is currently pursuing the Ph.D. degree.

Her current research interests include low-power electrochemical sensing interface circuits and analog-to-digital converter circuits.



YUPING DENG received the B.S. degree from the University of Science and Technology Beijing, Beijing, China, in 2018. He is currently pursuing the Ph.D. degree in materials science and engineering with Tsinghua University, Beijing.

He joined Dr. Lan Yin's research group in 2018. His research interests include organic electronics and biosensors.



CHAO XIE received the B.S. degree in electronic science and technology from the Huazhong University of Science and Technology, Wuhan, China, in 2018. He is currently pursuing the Ph.D. degree with Tsinghua University, Beijing, China.

His research interests focus on piezoelectric energy-harvesting systems and power management circuits.



MILIN ZHANG (Senior Member, IEEE) received the B.S. and M.S. degrees in electronic engineering from Tsinghua University, Beijing, China, in 2004 and 2006, respectively, and the Ph.D. degree from the Electronic and Computer Engineering Department, The Hong Kong University of Science and Technology, Hong Kong, in 2010.

She worked as a Postdoctoral Researcher with the University of Pennsylvania, Philadelphia, PA, USA, after finishing her doctoral studies. She joined Tsinghua University in 2016, where she

is an Associate Professor with the Department of Electronic Engineering. Her research interests include designing of various nontraditional imaging sensors and biomedical sensing applications.

Dr. Zhang has received the Best Paper Award of the BioCAS Track of the 2014 International Symposium on Circuits and Systems (ISCAS), the Best Paper Award (1st Place) of the 2015 Biomedical Circuits and Systems Conference (BioCAS), and the Best Student Paper Award (2nd Place) of ISCAS 2017. She serves and has served as the TPC Member for ISSCC, CICC, A-SSCC, and BioCAS. She is the Chapter Chair of the SSCS Beijing Chapter.

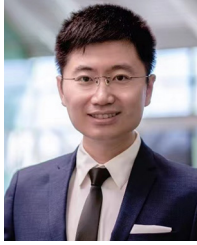


LAN YIN received the bachelor's degree in materials science and engineering from Tsinghua University, Beijing, China, in 2007, and the Ph.D. degree in materials science and engineering from Carnegie Mellon University, Pittsburgh, PA, USA, in 2011.

She is an Associate Professor with the School of Materials Science and Engineering, Tsinghua University. She has authored of over 40 journal papers and three book chapters. Her research interests are focused on biodegradable materials

and bioelectronics.

Dr. Yin received the Youth Thousand-Talent Award in 2015 and the Excellent Young Scholar Award from the National Natural Science Foundation of China in 2021, and is honored with the Chinese Materials Research Society the First Prize of Science and Technology Award.



XILIN LIU (Senior Member, IEEE) received the Ph.D. degree from the University of Pennsylvania, Philadelphia, PA, USA, in 2016.

He is currently an Assistant Professor with the University of Toronto, Toronto, ON, Canada. Before joining the University of Toronto in 2021, he held industrial positions with Qualcomm Inc., San Diego, CA, USA, where he conducted research and development of high-performance mixed-signal circuits for cellular communication.

He led and contributed to the IPs that have been integrated into products in high-volume production, including the industry's first 5G chipset. He was a Visiting Scholar with Princeton University, Princeton, NJ, USA, in 2014. He has coauthored two books along with over 30 peer-reviewed articles. His research interests include analog and mixed-signal IC design for emerging applications in healthcare and communication.

Dr. Liu was the first author of the papers that have received the Best Student Paper Award at the 2017 ISCAS, the Best Paper Award at the 2015 BioCAS, the Best Track Award at the 2014 ISCAS, and the Student Research Preview Award at the 2014 ISSCC. He also received the SSSC Predoctoral Achievement Award at the 2016 ISSCC.



JAN VAN DER SPIEGEL (Life Fellow, IEEE) received the master's degree in electromechanical engineering and the Ph.D. degree in electrical engineering from the University of Leuven, Leuven, Belgium, in 1974 and 1979, respectively.

He is a Professor of Electrical and Systems Engineering with the University of Pennsylvania, Philadelphia, PA, USA. He is the former Department Chair of Electrical Engineering, and an Associate Dean of Education and Professional Programs with the School of Engineering. He was

a Senior Visiting Professor with the Institute of Microelectronics and the Department of Electronics Engineering, Tsinghua University, Beijing, China, from September 2017 to February 2018. He has authored over 280 journal and conference papers and holds eight patents. His primary research interests are in mixed-mode VLSI design, smart sensors, CMOS vision sensors for polarization imaging, bioinspired image sensors, and brain-machine interfaces.

Prof. Van der Spiegel was the recipient of the IEEE Major Educational Innovation Award, the IEEE Third Millennium Medal, the UPS Foundation Distinguished Education Chair, and the Bicentennial Class of 1940 Term Chair. He received the IBM Young Faculty Development Award and the Presidential Young Investigator. He has served for several IEEE Program Committees, such as IEDM, ICCD, ISCAS, and ISSCC and was the Technical Program Chair of the 2007 International Solid-State Circuit Conference (IEEE ISSCC). He is an Associate Editor of the IEEE TRANSACTIONS ON BIOMEDICAL CIRCUITS AND SYSTEMS, a Section Editor of the *Journal of Engineering of the Institute of Engineering and Technology*, and a former member of the Editorial Board of the IEEE Proceedings. He was the President of the IEEE Solid-State-Circuits Society from 2016 to 2017, and General Conference Chair of the IEEE ISSCC in 2019 and 2020. He is a member of the Phi-Beta-Delta, Tau-Beta-Pi, and Eta-Kappa-Nu. He is a Distinguished Lecturer of the Solid-State Circuit Society.